

Stabilization and Destabilization of Multimode Solitons in Nonlinear Degenerate Multi-Pass Cavities

Junhan Huang^{1,2}, Bingbing Zhu^{1,2}, Shanyue Li^{1,2}, Kun Ding^{1,2}, and Zhensheng Tao^{1,2*}

¹ State Key Laboratory of Surface Physics, Key Laboratory of Micro and Nano Photonic Structures (MOE), and Department of Physics, Fudan University, Shanghai 200433, China.

² Shanghai Key Laboratory of Metasurfaces for Light Manipulation, Fudan University, Shanghai 200433, China.

*Corresponding author. Email: zhenshengtao@fudan.edu.cn.

Abstract

Optical solitons in multimode nonlinear optical systems offer a unique platform for exploring the interplay of nonlinearity, dispersion, and spatial mode coupling, offering insights into complex nonlinear wave phenomena. Multi-pass cavities (MPCs) incorporating nonlinear Kerr media serve as prototypical systems, enabling high-efficiency supercontinuum generation and pulse compression. However, stabilizing femtosecond laser pulses in solid-medium-based MPCs (solid MPCs) under high Kerr nonlinearity remains a significant challenge due to multimode coupling, which disrupts beam stability. In this work, we address this challenge by investigating the stability of laser pulses in MPCs using Floquet analysis and first-order perturbation theory. We identify novel mode-coupling-suppression (MCS) medium lengths, where destructive interference among multimode wave components suppresses coupling and facilitates soliton stabilization. Under MCS conditions, we demonstrate stable beam propagation in solid MPCs with nonlinear phases up to 1.85π per pass, achieving 10-fold pulse compression with exceptional spatio-spectral homogeneity. Our findings offer valuable guidance for designing advanced MPCs with tailored Kerr media.

Introduction

Solitons are self-sustained particle-like waves that widely exist in nonlinear systems. Understanding the mechanisms that stabilize optical solitons in multimode systems is essential because they underpin many unique nonlinear wave phenomena, such as spatial self-organization¹⁻³, soliton fission^{4,5}, and the emergence of spatiotemporal solitons, also known as “light bullets”^{6,7}. While multimode solitons have been extensively studied in optical fibers, free-space cavities offer a complementary platform with weak transverse mode confinement and outstanding suitability for high-energy applications^{8,9}. Free-space cavities also enable the exploration of diverse nonlinear regimes through precise dispersion control of cavity mirrors or by varying the nonlinear optical media.

Among free-space multimode nonlinear systems, multi-pass cavities (MPCs) incorporating nonlinear Kerr media represent a prototypical example. In recent studies, nonlinear MPCs have been successfully employed for supercontinuum generation and pulse compression. By circulating femtosecond laser pulses, MPCs achieve substantial spectral broadening, enabling high-throughput, and high-quality pulse compression with high power^{10,11}, high pulse energy¹¹, and few-cycle durations^{12,13}. Commonly used Kerr media include noble gases^{10,11,21-30,12,31-33,14-20}, and single^{13,34,43,44,35-42} or multiple⁴⁵⁻⁴⁹ solid media.

A key design criterion for nonlinear MPCs is to maximize the single-pass nonlinear phase (SNLP) while ensuring stable propagation of femtosecond laser pulses and maintaining high spatio-spectral beam quality. Achieving a larger SNLP reduces

the number of roundtrips needed to achieve sufficient spectral broadening, with current state-of-the-art nonlinear MPCs typically requiring 30–50 roundtrips. Fewer roundtrips can reduce the demand for costly broadband and high-efficiency optical coatings and mitigate instability caused by long optical paths. This challenge is fundamentally equivalent to identifying soliton solutions in nonlinear MPCs under strong Kerr nonlinearity. Of particular interest are discrete spatial solitons^{50,51} with consistent transverse spatial modes in the Kerr medium during each pass.

Experimentally, state-of-the-art nonlinear MPCs reveal a significant disparity between gas-filled and solid-medium-based MPCs (solid MPCs). Solid MPCs are limited to SNLP values below 0.8π , far lower than the 2π achievable in gas-filled MPCs (Fig. 1b). This limitation stems primarily from the degradation of spatio-spectral beam quality under high nonlinearity in solid MPCs, which poses significant constraints on their applications.

Previous theoretical studies have highlighted the role of multimode coupling in spatial degradation, both in single-pass setups⁵² and gas-filled MPCs^{53,54}. Soliton-like dynamics of the pulse propagation in solid MPCs have also been revealed at mid-infrared wavelengths³⁴. Coupled-mode theory, in particular, has shown that degenerate cavity geometries—where higher-order modes are phase-matched with the fundamental modes—strongly influence beam stability^{54,55}. This insight is practically important, as most nonlinear MPC implementations utilize degenerate cavity configurations, also known as "*q*-preserving" geometries^{56,57}. Despite these insights, the fundamental differences between solid and gas-filled MPCs, as well as the underlying mechanisms

that stabilize or destabilize multimode solitons, remain poorly understood.

In this work, from the perspective of multimode solitons, we investigate laser-pulse stability in nonlinear MPCs with strong Kerr nonlinearity. Using Floquet analysis and first-order perturbation theory, we elucidate the mechanisms by which multimode coupling, induced by the interplay between cavity degeneracy and Kerr nonlinearity, destabilizes solitons (Fig. 1c). Our results clarify the observed differences between gas-filled and solid MPCs. More importantly, for degenerate geometries, we identify novel *mode-coupling-suppression (MCS) medium lengths* (d_{MCS}), where destructive interference among multimode wave components within the Kerr medium suppresses multimode coupling. This stabilization mechanism facilitates soliton formation in degenerate nonlinear MPCs under high nonlinearity (Fig. 1c), with gas-filled MPCs emerging as a special case of the MCS condition.

Under the MCS condition, we demonstrate stable soliton propagation with a nonlinear phase up to $b=1.85\pi$ per pass in solid MPCs (star in Fig. 1b), resulting in pulse compression 10-fold pulse compression with exceptional spatio-spectral quality after only 10 roundtrips. This result far exceeds the SNLP limits of the existing solid MPCs, offering valuable insights for designing advanced nonlinear MPCs with tailored Kerr media.

Phase Diagrams of Beam-Propagation Stability

The conceptual schematic of a nonlinear MPC is shown in Fig. 1a. It consists of two concave mirrors (C.M.), each with a focal length F , separated by a distance of $2L$. At the cavity center, a Kerr medium with a length of $2d$ interacts with femtosecond laser

pulses, inducing an SNLP denoted as b . Here, the nonlinear phase is characterized by $b = \frac{2\pi}{\lambda_0} n_2 \int_{-d}^d I(z) dz$, where λ_0 is the laser wavelength, n_2 is the nonlinear refractive index, z is the coordinate along the cavity axis (with the origin at the cavity center), and $I(z)$ is the laser intensity within the Kerr medium.

To investigate laser-beam propagation stability, we perform full space-time-coupled nonlinear Schrödinger equation (NLSE) simulations⁵⁸ across various cavity geometries (characterized by F/L), Kerr-medium lengths (d/L), and SNLPs b [see Supplementary Materials (SM) Section S1]. We assess beam instability by evaluating the spatio-spectral homogeneity ($\langle V \rangle$) of the output beam⁴⁸ (see Methods). The two-dimensional phase diagrams of inhomogeneity are shown in Figs. 2a-c, where higher values represent stronger inhomogeneity.

Several key observations can be made. First, the spatio-spectral homogeneity improves as d/L increases. When $d/L \rightarrow 0$ (Fig. 2a), the simulation represents conditions typical of solid MPCs, where the medium length is much smaller than the cavity length. In the simulations, a medium length of $d=1$ mm is used. In contrast, $d/L=1.0$ (Fig. 2c) corresponds to a gas-filled MPC, where the gas medium occupies the entire cavity volume.

Second, for $d/L \rightarrow 0$ (Fig. 2a), cavities with higher degeneracy exhibit pronounced spatio-spectral inhomogeneity. Here, cavity degeneracy arises when the accumulated Gouy phases of the g - and n -th order Laguerre-Gaussian (LG) modes after a single pass satisfy $\xi_n = \xi_g + 2j\pi$, where j is an integer. Since Gaussian-profiled laser beams are usually used as inputs, the degree of degeneracy relative to the LG₀₀ mode

is of particular interest. The Gouy-phase condition $\xi_n = \xi_0 + 2j\pi$ leads to the following degeneracy condition:

$$4u \arctan\left(\frac{1}{\sqrt{2F/L-1}}\right) = 2v\pi, \quad (1)$$

where (u, v) are a pair of coprime integers ($v < u$), representing the cavity-degeneracy indices. For a Herriott-type MPC⁵⁹ in practice, the q -preserving configuration results in closed ray paths, where rays retrace their trajectories after a certain number of roundtrips^{55,56}. Under this condition, the degeneracy index u represents the total number of laser spots present on each cavity mirror (see inset of Fig. 1a). The index v indicates the position where the ray bounces after its first roundtrip (blue spot), assuming the incident beam initially hits spot #1 (green spot).

Quantitatively, the degree of cavity degeneracy can be characterized by a normalized density of states (DOS), which counts the number of LG modes that are degenerate with the LG₀₀ mode (Fig. 2d; see Methods). A clear correlation is observed between the DOS peaks and spatio-spectral inhomogeneity patterns (Fig. 2a). This observation is further corroborated by analyzing the spatio-temporal profiles for both degenerate (condition A) and non-degenerate (condition B) cases (Figs. 2e-f). Under the degenerate conditions, higher-order modes and pulse splitting are evident (Fig. 2e), indicating spatio-temporal instability.

Lastly, but more interestingly, we find that specific medium lengths, denoted as d_{MCS} , enable significant beam-quality improvement even under degenerate conditions. For instance, when $d_{\text{MCS}} = \frac{1}{3}L$ with $F/L=2/3$ and degeneracy indices $(u, v)=(3, 2)$ (condition C in Fig. 2b), the strong inhomogeneity observed in condition A (Fig. 2a) is

remarkably suppressed, resulting in a spatio-spectrally homogeneous output beam. The comparison between Figs. 2g and 2e further demonstrates that the spatio-temporal breakdown is mitigated under d_{MCS} .

To highlight this intriguing behavior, we further compare the zoomed-in views around the degenerate point ($F/L=2/3$) for both $d/L \rightarrow 0$ and $d=d_{\text{MCS}}$ (Figs. 2h-i). Clearly, at $d=d_{\text{MCS}}$, the inhomogeneity at the degenerate point is sharply suppressed, while the surrounding regions with lower DOS exhibit some inhomogeneity, forming a “V”-shape pattern around the degenerate point (Fig. 2i).

Notably, the high-homogeneity regions in Figs. 2a-c indicate the formation of discrete spatial solitons, where laser pulses maintain stable spatial profiles within the nonlinear medium or on the cavity mirrors (see SM Section S2). While our numerical simulations provide valuable insights into the stability landscape of these solitons, the underlying mechanisms remain complex. In the following, we employ analytical Floquet theory and perturbation theory to derive the stability criteria governing discrete spatial solitons in nonlinear MPCs.

Floquet Theory Analysis

To simplify the analysis, we begin by neglecting space-time coupling effects. Our results will show that this approximation can precisely predict the key stability criteria and serves as a valuable framework for their understanding. Given that an optical cavity represents the periodic propagation of a light beam in space, its behavior can be described using Floquet theory⁶⁰. For a linear cavity, the Floquet eigenequation is

$$\left[H_0(r, z) - i \frac{\partial}{\partial z} \right] |\Phi_{n,m}(r, z)\rangle = \varepsilon_{n,m} |\Phi_{n,m}(r, z)\rangle, \quad (2)$$

where H_0 is the linear-cavity Hamiltonian, $|\Phi_{n,m}\rangle$ is the Floquet eigenstate, and $\varepsilon_{n,m} = \varepsilon_n - m\Omega$ is the Floquet eigenvalue for the m -th replica of the n -th LG mode, with $\Omega = \pi/L$ being the Floquet “driving frequency”. Here, ε_n is the eigenvalue of the n -th LG mode, related to the single-pass Gouy phase by $\varepsilon_n = \xi_n/(2L)$. In the Floquet framework, cavity degeneracy occurs when the eigenvalue of the (n, m) -th state coincides with that of the fundamental LG₀₀ mode (Fig. 1c), i.e. $\varepsilon_{n,m} = \varepsilon_{0,0}$, which yields the same degeneracy condition as in Eq. (1). We note that, due to the periodic nature of beam propagation, a degenerate cavity characterized by degeneracy indices (u, v) supports an infinite number of degenerate modes, with their indices (n, m) being integer multiples of (u, v) .

To analyze a nonlinear MPC, we apply perturbation theory by expanding the ground-state eigenfunction in the Floquet basis: $|\Psi_{0,0}\rangle = \sum_{n,m} C_{n,m} |\Phi_{n,m}\rangle$, where the expansion coefficients $C_{n,m}$ are given by

$$C_{n,m} = \frac{-b c_{0,0} |c_{0,0}|^2 \Theta_{n,m}(d)}{\varepsilon_{0,0} - \varepsilon_{n,m}}. \quad (3)$$

The overlap integral $\Theta_{n,m}(d)$ is defined as

$$\Theta_{n,m}(d) = \frac{1}{2d_{\text{eff}}} \left\langle \Phi_{n,m} \left| S(z, d) \left| \Phi_{0,0} \right|^2 \right| \Phi_{0,0} \right\rangle, \quad (4)$$

where $d_{\text{eff}} = z_0 \arctan\left(\frac{d}{z_0}\right)$ defines an effective medium length⁵⁶, with z_0 being the Rayleigh distance, and $S(z, d)$ is a periodic Heaviside function defining the Kerr-medium regions. Within the Floquet framework, the expansion coefficient of the LG_{0n} mode is given by $c_n = \sum_m C_{n,m}$. A detailed derivation is provided in Methods.

Using this perturbative approach, we compute the eigenstates of nonlinear MPCs for various cavity geometries and medium lengths (conditions A, B, and C in Figs. 2a-

c) under an SNLP $b=0.5$ rad. For a nearly degenerate solid MPC with $F/L=0.663$ [close to the degenerate condition A with $F/L=2/3$ and $(u, v)=(3, 2)$], the radial profile of the eigenstate ($|U(r)|$) deviates from a Gaussian shape, exhibiting ripples at large radii (Fig. 3a). The spatial-mode expansion reveals significant contributions from the higher-order LG modes (Fig. 3b). To validate the perturbation approach, we numerically compute the eigenstate profiles using the Fox-Li iteration algorithm^{50,61} (red lines and symbols in Figs. 3a-b; see SM Section S3). Although some discrepancies arise when b is large, the perturbative approach effectively captures the emergence of higher-order modes with accurate indices. Further stability analysis (see SM Section S4) shows that multimode coupling in degenerate MPCs significantly disrupts stable propagation of the eigenstate (Fig. 3c), indicating that cavity degeneracy hinders soliton stabilization.

In contrast, under the non-degenerate condition B ($F/L=0.8$), the eigenstate maintains a nearly Gaussian profile (Fig. 3d), with the expansion coefficients showing negligible contributions from higher-order modes (Fig. 3e). The eigenstate exhibits stable discrete-soliton modes in the non-degenerate solid MPC (Fig. 3f).

The stark contrast between the degenerate and non-degenerate MPCs (Figs. 3a-f) is consistent with the phase diagram shown in Fig. 2a and can be explained by Eq. (3). When $d/L \rightarrow 0$, the overlap integral $\Theta_{n,m}$ is typically non-zero. Consequently, the degenerate condition ($\varepsilon_{0,0} = \varepsilon_{n,m}$) causes the expansion coefficient $C_{n,m}$ to diverge, driving substantial energy transfer from the LG₀₀ mode to higher-order modes. We note that, while previous studies have revealed the importance of multimode coupling in degrading beam quality in degenerate MPCs^{54,55}, our results provide a novel perspective

based on discrete multimode solitons, offering a comprehensive understanding of the underlying mechanisms.

For condition C, where the cavity is nearly degenerate but the medium length is $d=d_{\text{MCS}}$, our Floquet analysis reveals negligible multimode coupling (Figs. 3g-h), and the eigenstate represents a soliton mode that propagates stably within the nonlinear MPC (Fig. 3i). This observation is consistent with Fig. 2b and can be attributed to the diminishing of the overlap integral $\Theta_{n,m}(d)$ in Eq. (3). Accordingly, we refer this specific medium length as the mode-coupling-suppression (MCS) length.

Mechanisms for MCS Medium Length

For a degenerate mode (n, m) , $\Theta_{n,m}(d)$ in Eq. (4) can be calculated analytically. For a given degenerate cavity with indices (u, v) , the multimode coupling is suppressed only when the expansion coefficients of all the degenerate modes (n, m) , derived from (u, v) , vanish ($C_{n,m}=0$). By setting $\Theta_{n,m}(d) = 0$, we obtain d_{MCS} :

$$4u \arctan\left(\frac{d_{\text{MCS}}/L}{\sqrt{2F/L-1}}\right) = 2k\pi, \quad k = 1, 2, \dots, v, \quad (5)$$

where the left-hand side represents the accumulated Gouy phase difference within the Kerr medium. Equation (5) tells that for each (u, v) , there are v distinct d_{MCS} values that satisfy this condition. A detailed derivation is provided in SM Section S5. In Figs. 4a, we use $(u, v)=(4, 3)$ as an example, and plot the Gouy-phase differences [Eq. (5)] and $\Theta_{n,m}(d)$, with the corresponding d_{MCS} values indicated.

Figure 4a also explains why gas-filled MPCs can support high-quality beam propagation and efficient nonlinear light-matter interaction. First, the coefficients $C_{n,m}$ generally decrease oscillatory with increasing d/L . This behavior is analogous to phase-

matching in nonlinear optics⁶², where a thicker nonlinear medium leads to destructive interference among multimode wave components. Second, in degenerate cavities, $d/L=1$ always results in vanishing overlap integrals for all the degenerate modes (n, m) , effectively suppressing multimode coupling. Therefore, gas-filled MPCs can be regarded as a special case of the MCS condition.

The MCS condition facilitates high SNLPs by employing the medium length $d=d_{\text{MCS}}$ to suppress multimode coupling. We conduct numerical simulations with b approaching 1.85π per pass, which significantly exceeds the existing solid MPC compressors (star in Fig. 1b). For simplicity, we neglect material dispersion in the simulation. The initial pulse duration is 170 fs with a pulse energy of 1.32 μJ . The MPC operates under the degenerate condition with $F=21.6$ cm, $L=39.75$ cm, and $(u, v)=(11, 9)$. Accordingly, we set the medium length to $2d_{\text{MCS}}=26.9$ cm, and the material is fused silica.

In Fig. 4b, we present the transverse beam profiles over 20 passes (10 roundtrips), demonstrating stable propagation. We note that the chosen MPC geometry allows a practical Herriott-type MPC design with small mirrors that enable beam injection and extraction without intersecting the beam path. Furthermore, because the overlap integral Θ is small near $d=d_{\text{MCS}}$, the beam quality remains robust against small variations in medium length around d_{MCS} . For comparison, using a thin fused-silica plate ($d=1.0$ mm), as commonly employed in previous studies, destabilizes beam propagation after only 5 roundtrips (Fig. 4c), leading to severe degradation in beam quality.

Stable beam propagation allows continuous accumulation of nonlinear phases, with the total accumulated phase reaching 116.2 rad after 10 roundtrips. The resultant spectral bandwidth is sufficient for direct pulse compression from 170 fs to ~ 13.2 fs (Fig. 4d), achieving >10 -fold compression in a single-stage all-solid MPC compressor. High spatio-spectral homogeneity can be maintained even under such strong nonlinearity, reaching $\langle V \rangle \approx 0.95$ (Fig. 4e).

Discussion and Conclusion

We note that the above analysis is based on Floquet analysis without considering space-time coupling effects. Space-time coupling can modify the stability landscape. One particular example is that, in gas-filled MPCs with $d/L=1$, spectro-spatial inhomogeneity still presents at large nonlinearity in cavities slightly deviating from the degenerate points (Fig. 2c). Such disruption can also be observed in solid MPCs. This behavior can be attributed to space-time coupling during nonlinear propagation, which disrupts the ideal destructive interference conditions ($\Theta_{n,m}=0$), thereby affecting the beam stability.

In addition to the limitations imposed by multimode coupling, the strength of nonlinearity in MPCs is constrained by the peak power reaching the critical power for self-focusing $P_0/P_{\text{crit}} < 1^{63}$. Under this constraint, for a degenerate MPC with indices (u, v) operating under the MCS condition, the SNLP is limited by:

$$b < \frac{2k\pi}{u}, \quad k = 1, 2, \dots, v. \quad (6)$$

Detailed derivations are provided in Methods. Equation (6) offers valuable insights for maximizing SNLP in degenerate nonlinear MPCs. First, smaller degeneracy indices $(u,$

ν) allow for higher SNLP. However, in Herriott-type configurations, a smaller u -index reduces the total number of roundtrips, thereby limiting the total nonlinear phase accumulation. This limitation may be circumvented by adopting alternative cavity configurations¹⁹. Second, selecting large k -indices enhances the achievable SNLP. Notably, the condition of $k=\nu$ corresponds to gas-filled MPCs, where Eq. (6) is consistent with previous studies⁵⁶.

Although Eq. (6) underscores the superior performance of gas-filled MPCs, solid MPCs potentially offer significant flexibility through the tailored design of nonlinear optical media. While our study focuses on a single bulk Kerr medium placed at the cavity center, the same MCS mechanism can be extended to configurations involving multiple periodic or nonperiodic, centro-symmetric, or asymmetric distributions of Kerr media. Various MPC geometries beyond the Herriott-type configuration can also be explored. These advancements open up new possibilities for applications of optical cavities in supercontinuum generation and other nonlinear processes.

In conclusion, we have investigated the stability of multimode solitons in nonlinear MPCs with strong Kerr nonlinearity. Using Floquet analysis and first-order perturbation theory, we elucidated the critical role of multimode coupling in soliton destabilization. Importantly, we identified the novel MCS condition that enables soliton stabilization in degenerate MPCs with a nonlinear phase of up to 1.85π per pass in solid MPCs, significantly exceeding the current state-of-the-art. Our findings provide a unified framework that explains the disparity between gas-filled and solid MPCs, offering new opportunities for advanced nonlinear MPCs with tailored Kerr media for

high-power and high-efficiency ultrafast applications.

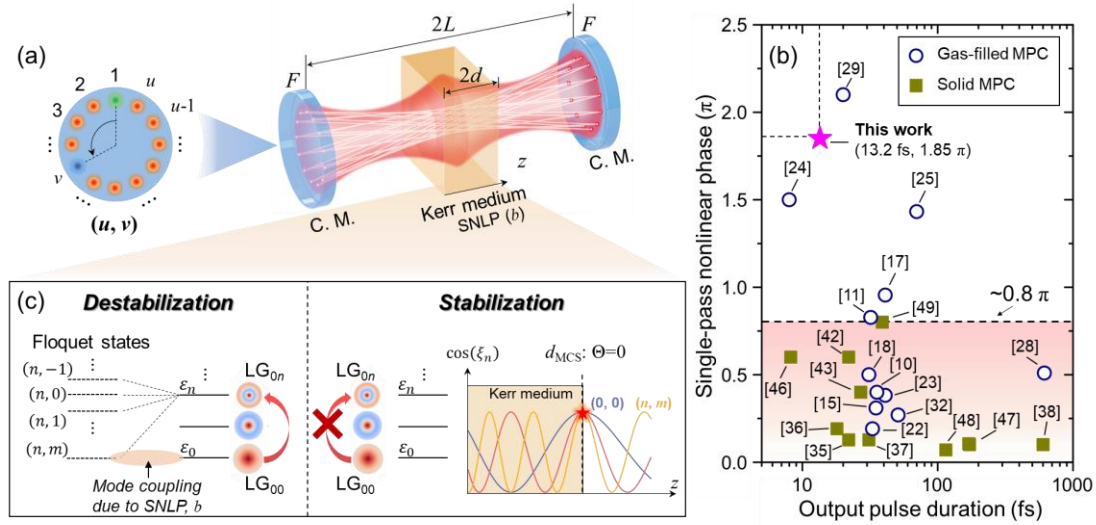


Figure 1. Mechanisms of stabilization and destabilization of multimode solitons in nonlinear MPCs. (a) Schematic of a nonlinear MPC geometry. C.M.: Concave mirror.

Inset: Laser-spot distribution on a Herriott-type MPC with a degeneracy defined by indices (u, v) . The green spot marks the initial position where the incident laser beam strikes, while the blue spot indicates its position after the first roundtrip. (b) Summary of state-of-the-art nonlinear MPCs for supercontinuum generation and pulse compression. The dashed line indicates the SNLP limit of existing solid MPCs. (c) Mechanisms underlying the stabilization and destabilization of multimode solitons in nonlinear MPCs.

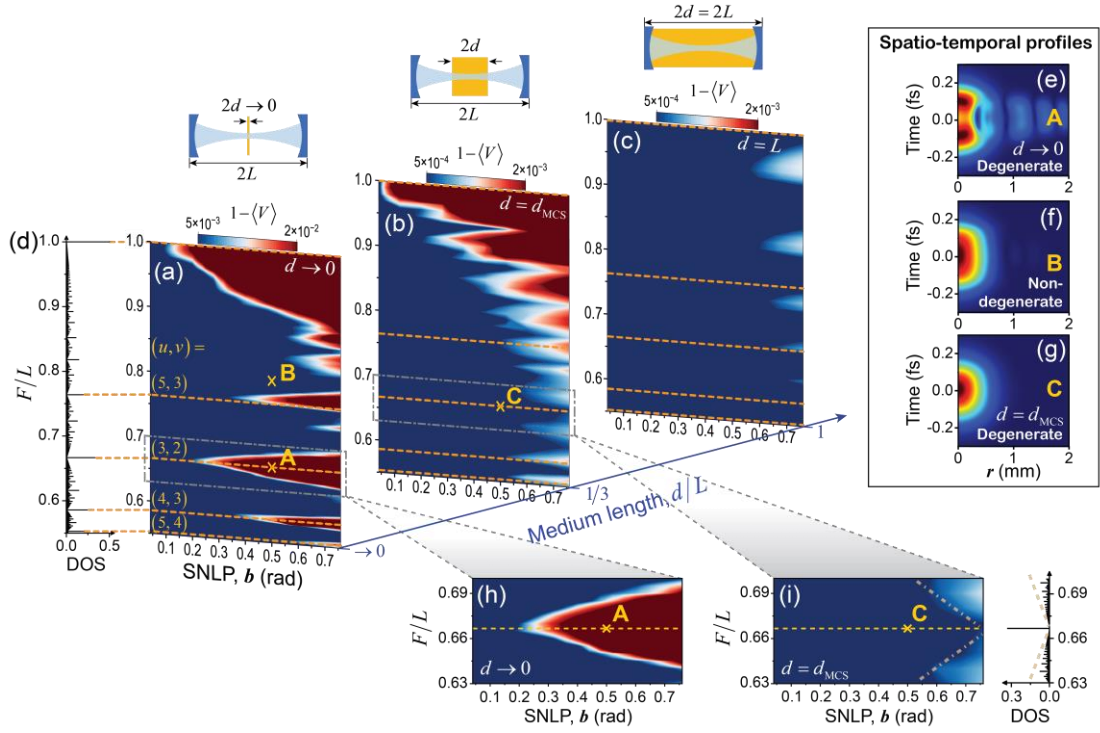


Figure 2. Stabilization landscape of nonlinear MPCs. (a-c) Phase diagrams of output beam inhomogeneity as a function of cavity geometry F/L and SNLP b , for medium length d/L corresponding to (a) a thin plate ($\rightarrow 0$), (b) the MCS length (d_{MCS}), and (c) a gas-filled MPC ($d=L$). Conditions of A, B, and C are labeled. Dashed lines indicate degeneracy geometries with $(u, v)=(5, 3)$, $(3, 2)$, $(4, 3)$, and $(5, 4)$. (d) DOS as a function of F/L , with the DOS peaks corresponding to the degeneracy geometries (dashed lines). (e-g) Spatio-temporal profiles of the output beams after 20 roundtrips for Condition A, B, and C, as labeled in (a-c). (h-i) Zoomed-in views of the phase diagrams near the degeneracy point $(u, v)=(3, 2)$, as illustrated by the dashed-dotted boxes in (a-b). DOS results for the same F/L region are shown in the right panel.

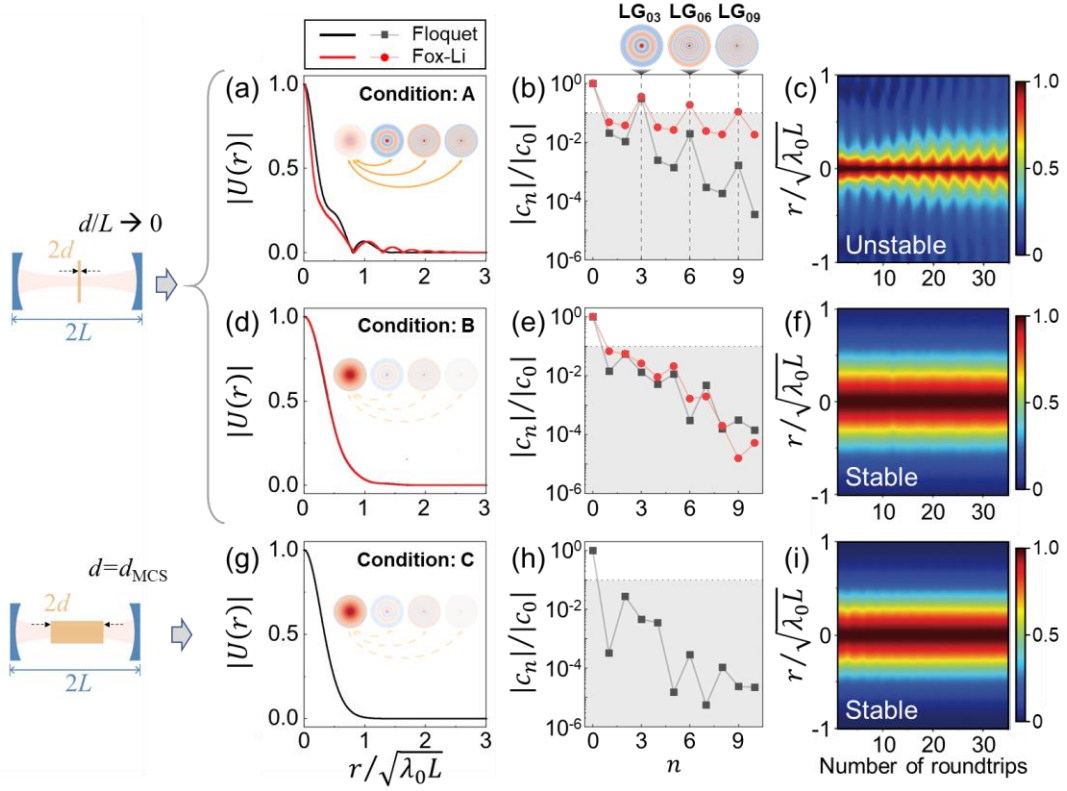


Figure 3. Stabilization and destabilization of multimode solitons. (a) Radial profiles of the eigenstate for a nearly degenerate solid MPC with $F/L=0.663$ (close to Condition A) with SNLP $b=0.5$, obtained from Floquet analysis (black line) and the Fox-Li algorithm (red line). **Inset:** Illustration of energy transfer from the LG_{00} mode to higher-order LG modes. (b) Normalized expansion coefficients $|c_n|/|c_0|$ of the eigenstates shown in (a). The horizontal dashed line indicates the amplitude of $|c_n|$ being 10% of the amplitude of the fundamental mode $|c_0|$. The LG modes of LG_{03} , LG_{06} , and LG_{09} are labeled. (c) Stabilization analysis of the eigenstate shown in (a). (d-f) Same as (a-b), but for the results at Condition B. (g-h) Same as (a-b), but for the results near Condition C.

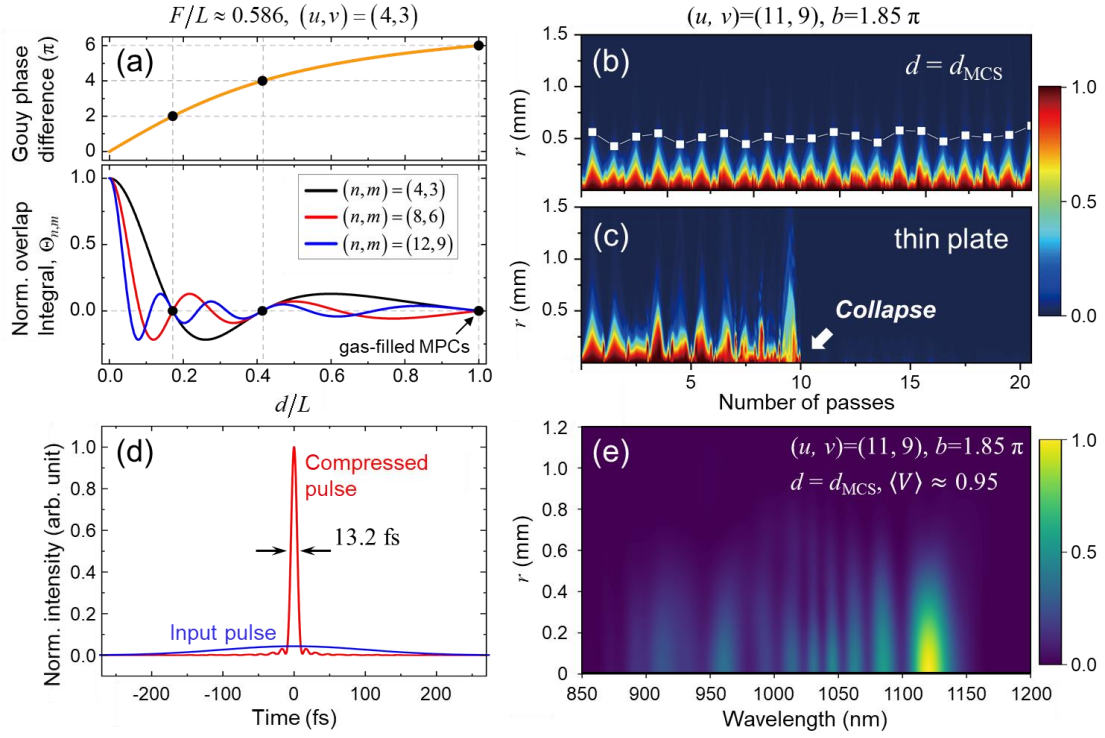


Figure 4. MCS mechanism stabilizing soliton propagation. (a) Gouy phase difference and normalized overlap integral $\Theta_{n,m}$ as a function of d/L for $F/L=0.586$ and $(u, v)=(4, 3)$. Dashed lines indicate the medium lengths where the Gouy phase accumulates by integer multiples of 2π , and $\Theta_{n,m}=0$ for all degenerate modes. (b) Simulated propagation of femtosecond laser pulses within a degenerate cavity with $(u, v)=(11, 9)$ under SNLP $b=1.85\pi$ and medium length $d=d_{MCS}$. Beam radii on a cavity mirror are indicated by symbols. (c) Same simulation conditions and cavity geometry as (b), but for a thin-plate Kerr medium. (d) Temporal profile of the compressed output pulse (red line) corresponding to the spectrum obtained from the simulation shown in (b). The blue line indicates the temporal profile of the input pulse. (e) Radial distribution of the output pulse spectrum obtained from the simulation in (b).

Methods

Spatio-spectral inhomogeneity. Quantitatively, the spatio-spectral homogeneity can

be characterized by the spectral overlap integral⁴⁸ $V(r) = \frac{\{\int_{\lambda} [I(\lambda, r)I(\lambda, 0)]^{1/2} d\lambda\}^2}{\int_{\lambda} I(\lambda, r) d\lambda \cdot \int_{\lambda} I(\lambda, 0) d\lambda}$, where

$I(\lambda, r)$ represents the spectral intensity of the output beam at radial coordinate r . The average overlap integral across the output beam is given by $\langle V \rangle = \frac{\int V(r) I(r) r dr}{\int I(r) r dr}$.

Floquet theory. We begin with the simplified NLSE is given by

$$i \frac{\partial U}{\partial z} = -\frac{1}{2n_0 k_0} \nabla_{\perp}^2 U + V_l(r, z)U + bV_k(r, z, U)U, \quad (7)$$

where the cavity-mirror potential $V_l(r, z)$ is given by

$$V_l(r, z) = \frac{\pi r^2}{\lambda_0 F} \sum_n \delta(z - (2n + 1)L), \quad (8)$$

and the Kerr nonlinear term $V_k(r, z, U)$ is

$$V_k(r, z, U) = -n_2 k_0 I_0(z = 0) S(z, d) |U|^2 \equiv -\frac{1}{2d_{\text{eff}}} S(z, d) |U|^2. \quad (9)$$

Here, $V_l(r, z)$ represents the cavity-mirror effect modeled using the thin-lens approximation. $V_k(r, z, U)$ describes the self-focusing effect induced by Kerr nonlinearity. $S(z, d)$ is a periodic Heaviside function defining the medium length:

$$S(z, d) \equiv \begin{cases} 1, & |z| \leq d \\ 0, & \text{else} \end{cases}, \quad z \in [-L, L], \text{ and } S(z + 2L) = S(z). \quad (10)$$

For convenience, we define an effective length $2d_{\text{eff}} = 2z_0 \arctan(d/z_0)$, where z_0 is the Rayleigh distance⁵⁶. The nonlinear phase per pass is then given by

$$b = n_2 k_0 I_0 \cdot 2d_{\text{eff}}. \quad (11)$$

We use Floquet theory to analyze the linear contribution in Eq. (7). The linear Hamiltonian is given by $H_0(r, z) = -\frac{1}{2n_0 k_0} \nabla_{\perp}^2 + V_l(r, z)$, and the corresponding Floquet eigenequation is:

$$\left[H_0(r, z) - i \frac{\partial}{\partial z} \right] |\Phi_n(r, z)\rangle = \varepsilon_n |\Phi_n(r, z)\rangle. \quad (12)$$

Since the Floquet Hamiltonian is periodic along z , its eigenstate $|\Phi_n(r, z)\rangle$ has an infinite number of replicas, $|\Phi_{n,m}(r, z)\rangle$, with Floquet eigenvalue $\varepsilon_{n,m} = \varepsilon_n - m\Omega$, where $\Omega = \pi/L$ is the “driving frequency”.

In the subspace with zero angular momentum, the Floquet state is expressed as

$$|\Phi_{n,m}(r, z)\rangle = \frac{\sqrt{2/\pi}}{w(z)} L_n \left[2 \frac{r^2}{w^2(z)} \right] e^{-\frac{r^2}{w^2(z)}} e^{-ik\frac{r^2}{2R(z)}} e^{-i\frac{1}{2}\xi_n(z) + i\frac{\xi_n(L)}{2L}z - im\Omega z} \equiv \psi_n(r, z) e^{i\frac{\xi_n(L)}{2L}z - im\Omega z}, \quad (13)$$

where $\psi_n(r, z) = \frac{\sqrt{2/\pi}}{w(z)} L_n \left[2 \frac{r^2}{w^2(z)} \right] e^{-\frac{r^2}{w^2(z)}} e^{-ik\frac{r^2}{2R(z)}} e^{-i\frac{1}{2}\xi_n(z)}$ is the linear-cavity eigenstate, also known as the LG_{0n} mode, L_n represents the n -th order Laguerre polynomial, $\xi_n(z)$ is the Gouy phase of the LG_{0n} mode:

$$\xi_n(z) = 2(2n + 1) \arctan\left(\frac{z/L}{\sqrt{2F/L-1}}\right). \quad (14)$$

The accumulated Gouy phase upon one pass through the cavity is $\xi_n(L)$. The Floquet eigenvalue, thus, is given by:

$$\varepsilon_{n,m} = \frac{\xi_n(L)}{2L} - m\Omega. \quad (15)$$

Cavity degeneracy occurs when the eigenvalue of (n, m) -th state coincides with that of the ground state, $\varepsilon_{n,m} = \varepsilon_{0,0}$, which yields the same degeneracy condition as shown in Eq. (1).

Perturbation theory. We apply perturbation theory to derive the ground-state solitons in nonlinear MPCs. Since the soliton state shares the same periodicity as the cavity, the ground-state soliton $|\Psi_{0,0}(r, z)\rangle$ and its eigenenergy $\varepsilon_{0,0}$ can be expanded as a superposition of the Floquet eigenstates and eigenvalues:

$$|\Psi_{0,0}(r, z)\rangle = c_{0,0}|\Phi_{0,0}(r, z)\rangle + b \sum_{n' \neq 0, m' \neq 0} \tilde{c}_{n', m'} |\Phi_{n', m'}(r, z)\rangle, \quad (16)$$

$$\text{and } \varepsilon_{0,0} = \varepsilon_{0,0} + b\Delta_{0,0}. \quad (17)$$

Here, we introduce the perturbation terms by assuming $b \ll 1$. The nonlinear eigenequation is

$$\left[H(r, z) - i \frac{\partial}{\partial z} \right] |\Psi_{0,0}(r, z)\rangle = \varepsilon_{0,0} |\Psi_{0,0}(r, z)\rangle, \quad (18)$$

where the nonlinear Hamiltonian is $H(r, z) = H_0(r, z) + bV_k(r, z, U)$. By substituting Eqs. (16-17) into Eq. (18), we obtain

$$\sum_{n', m' \neq 0} (\varepsilon_{0,0} - \varepsilon_{n', m'}) b \tilde{C}_{n', m'} |\Phi_{n', m'}\rangle + b \Delta_{0,0} C_{0,0} |\Phi_{0,0}\rangle = V_k C_{0,0} |\Phi_{0,0}\rangle. \quad (19)$$

By taking the inner product with $\langle \Phi_{n,m} |$ and using the orthogonal relation of the Floquet eigenstates, we arrive

$$\tilde{C}_{n,m} = \frac{C_{0,0} \langle \Phi_{n,m} | V_k | \Phi_{0,0} \rangle}{\varepsilon_{0,0} - \varepsilon_{n,m}}. \quad (20)$$

We further evaluate the overlap integral:

$$\langle \Phi_{n,m} | V_k | \Phi_{0,0} \rangle = -\frac{1}{2d_{\text{eff}}} |C_{0,0}|^2 \langle \Phi_{n,m} | S(z, d) | \Phi_{0,0} \rangle^2 | \Phi_{0,0} \rangle \equiv -|C_{0,0}|^2 \Theta_{n,m}(d), \quad (21)$$

where

$$\Theta_{n,m}(d) = \frac{1}{2d_{\text{eff}}} \langle \Phi_{n,m} | S(z, d) | \Phi_{0,0} \rangle^2 | \Phi_{0,0} \rangle. \quad (22)$$

Numerically, $\Theta_{n,m}(d)$ can be calculated by

$$\Theta_{n,m}(d) = \frac{1}{2d_{\text{eff}}} \frac{\pi}{L} \int_{-d}^d \left(\int_0^{+\infty} \phi_n^*(r, z) |\phi_0(r, z)|^2 \phi_0(r, z) e^{i2n[\frac{1}{2}\xi_0(z) - \frac{\xi_0(L)}{2L}z] + im\Omega z} r dr \right) dz, \quad (23)$$

where $\phi_n(r, z) = \frac{\sqrt{2/\pi}}{w(z)} L_n \left[2 \frac{r^2}{w^2(z)} \right] e^{-\frac{r^2}{w^2(z)}} e^{-ik \frac{r^2}{2R(z)}}$. Equation (22) is an alias for Eq. (4)

in the main text.

Cavity degeneracy and density of states. In the Floquet framework, the normalized

DOS is defined as⁶⁰:

$$D(\varepsilon) = \frac{1}{N} \sum_{n,m} \delta(\varepsilon - \varepsilon_{n,m}), \quad (24)$$

where N is the total number of states. All distinct Floquet states can be indexed by eigenvalues within the first Floquet Brillouin zone (FBZ) $[\varepsilon_0, \varepsilon_0 + \Omega]$, For a degenerate

cavity, the DOS peaks at the degenerate eigenvalues, whereas for a non-degenerate cavity, it approaches zero as $N \rightarrow \infty$. Thus, for a cavity characterized by degenerate indices (u, v) , the DOS can be explicitly expressed as

$$D = \begin{cases} \frac{1}{u}, & \text{for a } (u, v) \text{ degenerate cavity} \\ 0, & \text{for a non-degenerate cavity} \end{cases} \quad (25)$$

Critical power constraint. The critical power for a Kerr medium is given by $P_{\text{crit}} \approx \lambda_0^2 / (2\pi n_0 n_2)^{63}$. According to Eq. (11), the incident power is related to SNLP by

$$P_0 = \frac{\pi w_0^2 \lambda_0 b}{8\pi n_0 n_2 d_{\text{eff}}}, \quad (26)$$

where w_0 is the beam waist. Applying the constraint $P_0/P_{\text{crit}} < 1$ leads to

$$b < \frac{4d_{\text{eff}}}{z_0}. \quad (27)$$

Using the definition of d_{eff} :

$$d_{\text{eff}} = z_0 \arctan\left(\frac{d/L}{\sqrt{2F/L-1}}\right), \quad (28)$$

we derive the upper limit of SNLP as:

$$b < 4 \arctan\left(\frac{d/L}{\sqrt{2F/L-1}}\right). \quad (29)$$

Finally, by substituting Eq. (5) under the MCS condition, we obtain Eq. (6) which defines the upper limit of SNLP.

Reference

1. LIU, Z., WRIGHT, L. G., CHRISTODOULIDES, D. N. & WISE, F. W. Kerr self-cleaning of femtosecond-pulsed beams in graded-index multimode fiber. *Opt. Lett.* **41**, 3675–3678 (2016).
2. Safaei, R. *et al.* High-energy multidimensional solitary states in hollow-core fibres. *Nat. Photonics* **14**, 733–739 (2020).
3. Krupa, K. *et al.* Spatial beam self-cleaning in multimode fibres. *Nat. Photonics*

- 11**, 237–241 (2017).
4. Wright, L. G., Renninger, W. H., Christodoulides, D. N. & Wise, F. W. Spatiotemporal dynamics of multimode optical solitons. *Opt. Express* **23**, 3492–3506 (2015).
 5. Zitelli, M. *et al.* High-energy soliton fission dynamics in multimode GRIN fiber. *Opt. Express* **28**, 20473 (2020).
 6. Brambilla, M., Maggipinto, T., Patera, G. & Columbo, L. Cavity light bullets: Three-dimensional localized structures in a nonlinear optical resonator. *Phys. Rev. Lett.* **93**, 203901 (2004).
 7. Silberberg, Y. Collapse of optical pulses. *Opt. Lett.* **15**, 1282–1284 (1990).
 8. Lilienfein, N. *et al.* Temporal solitons in free-space femtosecond enhancement cavities. *Nat. Photonics* **13**, 214–218 (2019).
 9. Wright, L. G., Renninger, W. H., Christodoulides, D. N. & Wise, F. W. Nonlinear multimode photonics: nonlinear optics with many degrees of freedom. *Optica* **9**, 824–841 (2022).
 10. Russbueldt, P. *et al.* Scalable 30 fs laser source with 530 W average power. *Opt. Lett.* **44**, 5222–5225 (2019).
 11. Pfaff, Y. *et al.* Nonlinear pulse compression of a 200 mJ and 1 kW ultrafast thin-disk amplifier. *Opt. Express* **31**, 22740–22756 (2023).
 12. Daniault, L. *et al.* Sub-2-cycle post-compression of multi-mJ energy Ti : sapphire laser pulses in a gas-filled multi-pass cell. *Opt. Lett.* **49**, 6833–6836 (2024).

13. Barbiero, G. *et al.* Efficient nonlinear compression of a thin-disk oscillator to 8.5 fs at 55 W average power. *Opt. Lett.* **46**, 5304–5307 (2021).
14. SCHULTE, J., SARTORIUS, T., WEITENBERG, J., VERNALEKEN, A. & RUSSBUELDT, P. Nonlinear pulse compression in a multipass cell. *Opt. Lett.* **41**, 4511–4514 (2016).
15. Russbueltdt, P., Mans, T., Weitenberg, J., Hoffmann, H. D. & Poprawe, R. Compact diode-pumped 11 kW Yb:YAG Innoslab femtosecond amplifier. *Opt. Lett.* **35**, 4169–4171 (2010).
16. Eisenbach, L. *et al.* Highly efficient nonlinear compression of mJ pulses at 2 μm wavelength to 20 fs in a gas-filled multi-pass cell. *J. Phys. Photonics* **6**, 035015 (2024).
17. Heyl, C. M. *et al.* High-energy bow tie multi-pass cells for nonlinear spectral broadening applications. *J. Phys. Photonics* **4**, 014002 (2022).
18. Daher, N. *et al.* Multipass cells: 1D numerical model and investigation of spatio-spectral couplings at high nonlinearity. *J. Opt. Soc. Am. B* **37**, 993–999 (2020).
19. SCHÖNBERG, A. *et al.* Compact, folded multi-pass cells for energy scaling of post-compression. *arXiv:2409.02542* (2024).
20. Khatri, D. *et al.* Carrier-envelope phase-stabilized ultrashort pulses from a gas-filled multi-pass cell. *Appl. Phys. Lett.* **125**, 094103 (2024).
21. Silletti, L. *et al.* Dispersion-engineered multi-pass cell for single-stage post-compression of an ytterbium laser. *Opt. Lett.* **48**, 1842–1845 (2023).

22. Gierschke, P. *et al.* Nonlinear pulse compression to 51-W average power GW-class 35-fs pulses at 2- μ m wavelength in a gas-filled multi-pass cell. *Opt. Lett.* **47**, 3511–3514 (2022).
23. Müller, M., Buldt, J., Stark, H., Grebing, C. & Limpert, J. Multipass cell for high-power few-cycle compression. *Opt. Lett.* **46**, 2678–2681 (2021).
24. Kaumanns, M., Kormin, D., Nubbemeyer, T., Pervak, V. & Karsch, S. Spectral broadening of 112 mJ, 1.3 ps pulses at 5 kHz in a LG10 multipass cell with compressibility to 37 fs. *Opt. Lett.* **46**, 929–932 (2021).
25. Grebing, C., Müller, M., Buldt, J., Stark, H. & Limpert, J. Kilowatt-average-power compression of millijoule pulses in a gas-filled multi-pass cell. *Opt. Lett.* **45**, 6250–6253 (2020).
26. Viotti, A.-L. *et al.* Temporal pulse quality of a Yb:YAG burst-mode laser post-compressed in a multi-pass cell. *Opt. Lett.* **46**, 4686–4689 (2021).
27. Balla, P. *et al.* Postcompression of picosecond pulses into the few-cycle regime. *Opt. Lett.* **45**, 2572–2575 (2020).
28. Ueffing, M. *et al.* Nonlinear pulse compression in a gas-filled multipass cell. *Opt. Lett.* **43**, 2070–2073 (2018).
29. Lavenu, L. *et al.* Nonlinear pulse compression based on a gas-filled multipass cell. *Opt. Lett.* **43**, 2252–2255 (2018).
30. Kaumanns, M. *et al.* Multipass spectral broadening of 18 mJ pulses compressible from 13 ps to 41 fs. *Opt. Lett.* **43**, 5877–5880 (2018).
31. Rueda, P., Videla, F., Witting, T., Torchia, G. A. & Furch, F. J. 8 fs Laser

- Pulses From a Compact Gas-Filled Multi-Pass Cell. *Opt. Express* **29**, 27004–27013 (2021).
32. Kramer, P. L. *et al.* Enabling high repetition rate nonlinear THz science with a kilowatt-class sub-100 fs laser source. *Opt. Express* **28**, 16951–16967 (2020).
 33. Guo, J. *et al.* Spatial mode cleaning and efficient nonlinear pulse compression to sub-50 fs in a gas-filled multipass cell. *Opt. Lett.* **49**, 4385–4388 (2024).
 34. Carlson, D. *et al.* Nonlinear post-compression in multi-pass cells in the mid-IR region using bulk materials. *Opt. Lett.* **47**, 5289–5292 (2022).
 35. Gröbmeyer, S. *et al.* Self-compression at 1 μm wavelength in all-bulk multi-pass geometry. *Appl. Phys. B Lasers Opt.* **126**, 159 (2020).
 36. Song, J. *et al.* Generation of 601 fs pulse from an 8 kHz Nd:YVO₄ picosecond laser by multi-pass-cell spectral broadening. *Chinese Opt. Lett.* **19**, 093201 (2021).
 37. Zhang, X. *et al.* Milli-Joule pulses post-compressed from 14 ps to 475 fs in bulk-material multi-pass cell based on cylindrical vector beam. *Chinese Phys. B* **32**, 104206 (2023).
 38. Barbiero, G. *et al.* Broadband terahertz solid-state emitter driven by Yb:YAG thin-disk oscillator. *J. Phys. B At. Mol. Opt. Phys.* **53**, 125601 (2020).
 39. Gröbmeyer, S., Brons, J., Seidel, M. & Pronin, O. Carrier-Envelope-Offset Frequency Stable 100 W-Level Femtosecond Thin-Disk Oscillator. *Laser Photonics Rev.* **13**, 1800256 (2019).
 40. Vicentini, E. *et al.* Nonlinear pulse compression to 22 fs at 15.6 μJ by an all-

- solid-state multipass approach. *Opt. Express* **28**, 4541–4549 (2020).
41. TSAI, C.-L. *et al.* Efficient nonlinear compression of a mode-locked thin-disk oscillator to 27 fs at 98 W average power. *Opt. Lett.* **44**, 4115–4118 (2019).
 42. NATILE, M. *et al.* CEP-stable high-energy ytterbium-doped fiber amplifier. *Opt. Lett.* **44**, 3909–3912 (2019).
 43. JARGOT, G. *et al.* Self-compression in a multipass cell. *Opt. Lett.* **43**, 5643–5646 (2018).
 44. Fritsch, K., Poetzlberger, M., Pervak, V., Brons, J. & Pronin, O. All-solid-state multipass spectral broadening to sub-20 fs. *Opt. Lett.* **43**, 4643–4646 (2018).
 45. Raab, A.-K. *et al.* Multi-gigawatt peak power post-compression in a bulk multi-pass cell at a high repetition rate. *Opt. Lett.* **47**, 5084–5087 (2022).
 46. Viotti, A.-L. *et al.* Few-cycle pulse generation by double-stage hybrid multi-pass multi-plate nonlinear pulse compression. *Opt. Lett.* **48**, 984–987 (2023).
 47. Song, J. *et al.* Generation of 172 fs pulse from a Nd: YVO₄ picosecond laser by using multi-pass-cell technique. *Appl. Phys. B Lasers Opt.* **127**, 50 (2021).
 48. Weitenberg, J. *et al.* Multi-pass-cell-based nonlinear pulse compression to 115 fs at 75 μ J pulse energy and 300 W average power. *Opt. Express* **25**, 20502–20510 (2017).
 49. Seidel, M. *et al.* Factor 30 Pulse Compression by Hybrid Multipass Multiplate Spectral Broadening. *Ultrafast Sci.* **2022**, 9754919 (2022).
 50. Zhang, S. *et al.* Solitary beam propagation in periodic layered Kerr media enables high-efficiency pulse compression and mode self-cleaning. *Light Sci.*

- Appl.* **10**, 53 (2021).
51. Towers, I. & Malomed, B. A. Stable (2+1)-dimensional solitons in a layered medium with sign-alternating Kerr nonlinearity. *J. Opt. Soc. Am. B* **19**, 537–543 (2002).
 52. Milosevic, N., Tempea, G. & Brabec, T. Optical pulse compression: bulk media versus hollow waveguides. *Opt. Lett.* **25**, 672–674 (2000).
 53. Ueffing, M. Direct Amplification of Femtosecond Pulses. (Ludwig-Maximilians-Universität, 2018).
 54. Russbueltdt, P., Weitenberg, J., Vernaleken, A., Sartorius, T. & Schulte, J. METHOD AND ARRANGEMENT FOR SPECTRAL BROADENING OF LASER PULSES FOR NON-LINEAR PULSE COMPRESSION. (2017).
 55. Hanna, M. *et al.* Nonlinear Optics in Multipass Cells. *Laser Photonics Rev.* **15**, 2100220 (2021).
 56. Viotti, A.-L. *et al.* Multi-pass cells for post-compression of ultrashort laser pulses. *Optica* **9**, 197–216 (2022).
 57. Sennaroglu, A. & Fujimoto, J. Design criteria for Herriott-type multi-pass cavities for ultrashort pulse lasers. *Opt. Express* **11**, 1106–1113 (2003).
 58. Bergé, L., Skupin, S., Nuter, R., Kasparian, J. & Wolf, J. P. Ultrashort filaments of light in weakly ionized, optically transparent media. *Reports Prog. Phys.* **70**, 1633–1713 (2007).
 59. Herriott, D., Kogelnik, H. & Kompfner, R. Off-Axis Paths in Spherical Mirror Interferometers. *Appl. Opt.* **3**, 523–526 (1964).

60. Rudner, M. S. & Lindner, N. H. The Floquet Engineer's Handbook.
arXiv:2003.08252 (2020).
61. Fox, A. G. & Li, T. Resonant Modes in a Maser Interferometer. *Bell Syst. Tech. J.* **40**, 453–488 (1961).
62. Boyd, R. W. *Nonlinear Optics*. (Academic Press, Inc., 2008).
63. Fibich, G. & Gaeta, A. L. Critical power for self-focusing in bulk media and in hollow waveguides. *Opt. Lett.* **25**, 335–337 (2000).